WIDER Working Paper 2015/152

Assessing the likelihood of regional climate change over the Nile River basin and northern Africa

A hybrid assessment

C. Adam Schlosser[1*] and Ken Strzepek[1]

December 2015

UNU-WIDER

30 YEARS OF RESEARCH FOR DEVELOPMENT

wider.unu.edu

Abstract: Projections of regional changes in surface air temperature and precipitation for the greater Nile River basin and northern Africa are presented. The probabilistic projections are obtained through a technique that combines projections of the MIT Integrated Global System Model with climate-change patterns of the Intergovernmental Panel on Climate Change. Overall, the most consistent response to climate policy is seen in the distributions of temperature change. For precipitation, the predominant climate stabilization response is to reduce the likelihood of modal change. To quantify risks of climate change, the study data can be vetted through a chain of impact models.

Keywords: climate change, probability, northern Africa, Nile

Figures: at the end of the paper.

---

[1]MIT Joint Program for the Science and Policy of Global Change, Cambridge, MA, United States; *corresponding author: casch@MIT.EDU.

1   Introduction

Considerable attention has been paid to the fate of developing nations under climate change. An underpinning issue is whether any given region or nation of interest is under serious threat from anticipated climate change and the extent to which climate change mitigation policies reduce these threats and whether adaptation actions are required. In this study, we analyse the likelihood of changes in precipitation and surface air temperature through the middle of the twenty-first century for the greater Nile River basin as well as northern Africa. The distributions of climate change are constructed for an assessment of economic shocks to the basin. In the next section, the regions of focus and analytic approach are outlined. We present the technique used to construct pattern kernels of climate change based on information of regional change from climate models and the application of these patterns of change to downscale the zonal output of the MIT Integrated Global System Model (IGSM) (Sokolov et al. 2005). Given the large-ensemble approach employed by the IGSM, the fusion of these pattern kernels to the IGSM simulations results in frequency (or likelihood) distributions. We evaluate these for a selected region of interest, the Nile River basin, and evaluate the shifts in these derived distributions from an unconstrained emissions (UCE) scenario to a moderate climate stabilization policy. We close with concluding remarks and directions for future work and applications.

2   Characteristics of regional climate shifts

2.1   Greater Nile River basin

The greater Nile River basin (Figure 1) is one area of focus for this risk-based assessment of regional climate change. In addition, northern Africa is also summarized. These two regions, which complement a previous analysis of southern Africa, flank the Congo and greater Zambezi River basins (Schlosser et al. 2013; Schlosser and Strzepek 2013). As such, these analyses collectively serve to provide a more geographically comprehensive likelihood assessment of regional climate changes over northern Africa. The two climate variable inputs of interest herein are precipitation and near-surface air temperature (T_a). As described in Schlosser et al. (2013), many impact models are configured to resolve the major sub-basins and demographic regions of the basin, and the climate variables considered in this study are at a 2°×2° grid resolution. Overall, the Nile region and northern African experience distinct seasonal hydro-climates. The warmest temperatures are seen in the central portion of the Nile River basin and the strongest seasonality of temperature is located over the northern-most portion of the Nile region (Figure 2). The more persistent cooler temperatures lie within the central and eastern flanks of the Nile focus area (boxed area in Figure 2). Over many parts of the basin and focus region, a weak to modest seasonal swing in temperature is experienced and is in the order of 2–6°C; the strongest seasonal amplitudes in the order of 10°C are found in the central parts of the basin.

Northern Africa and the Nile region display distinct patterns and seasonal progression of precipitation (Figure 3). The southern region of the Nile River basin's seasonality is largely dictated by the progression of the inter-tropical convergence zone (ITCZ). The driest season occurs during the northern hemisphere winter (December–February, DJF), and higher rates of rain in the year are clearly seen during seasons in which the ITCZ prominently aligns itself over the southern and central portion of the basin. During June–August (JJA), precipitation maxima associated with the ITCZ progresses into the central portion of the basin; the southern portion of the basin experiences a double seasonal peak in precipitation during March–May (MAM), and September–November (SON) is associated with the northerly advance and retreat of the ITCZ. The northern regions of the Nile remain consistently dry during the entire year. However, the

eastern flank of the northern portion of the basin experiences its driest part of the year during JJA, and comparable (but weak) precipitation rates persist throughout the remainder of the year. Overall, MAM displays the most distinct north–south precipitation dipole, with widespread drier and wetter conditions, respectively. The most widespread and driest conditions across the basin occur during DJF. Given the strong seasonal features seen in the climatology of this region, subsequent analyses of the distributions constructed will focus on the seasonal aspects of change.

2.2 Regional climate change pattern kernels

Our construction of these distributions follows previous work presented by Schlosser et al. (2013). The underlying motivation for this approach is driven by the IGSM (Sokolov et al. 2009; Webster et al. 2012) that provides probabilistic projections of T_a and precipitation at the zonal level of detail. To add regional texture to these outcomes, we must expand this information across longitudes. To do this we use a Taylor expansion technique, described in detail by Schlosser et al. (2013). This transformation results in the construction of climate change pattern kernels. These kernels are scaled by global temperature change, and the numerical relationship can be expressed as:

$$V_{x,y}^{IGSM}(\Delta T\, V_{x,y}^{IGSM}\left(\mathrm{D}T_{Global}\right) = C_{x,y}\big|_{t_0}\, \overline{V}_y^{IGSM} + \left[\frac{dC_{x,y}}{dT_{Global}}\mathrm{D}T_{Global}^{IGSM}\right]\overline{V}_y^{IGSM},\qquad(1)$$

where $C_{x,y}\big|_{t_0}$ is the climatological downscaling transformation coefficient (taking the zonal mean to a particular longitudinal point) for any reference time period; we base this climatological coefficient on observational data. The project change in global temperature, ΔT_{Global}, is relative to the reference or climatological period. The derivatives of these transformation coefficients, $dC_{x,y}/dT_{Global}$, for any point (x,y) are discretely estimated from climate model information (for further details, see Schlosser et al. 2013). Therefore, the $dC_{x,y}/dT_{Global}$ terms serve as 'pattern kernels' of regional climate shifts. We construct a set of these pattern kernels based on the results of the Coupled Model Intercomparison Project Phase 3 (CMIP3, Meehl et al. 2007), which provides the regional basis for the large ensembles that allow us to construct distributions of change.

Precipitation

The multi-model mean of $dC_{x,y}/dT_{Global}$ for precipitation (Figure 4) indicates that, for the Nile River basin, the most notable shifts in regional precipitation are in the form of relatively wetter conditions over the southeast quadrant of the Nile region (with respect to its corresponding zonal mean), as seen by the positive $dC_{x,y}/dT_{Global}$ values that indicate relatively stronger precipitation rates with respect to the zonal mean as global climate warms. For the remainder of northern Africa, the strongest signature is seen along the equatorial region in the relatively drier conditions that persist for most of the year, but the strongest reduction is seen during MAM and coincides with the location of the ITCZ within the sub-basin. This correspondence, though slightly weaker, is also the case during SON. Throughout the remainder of northern Africa, the most notable signature across the mean of the model-based pattern kernels is a relative drying (i.e. reduced precipitation rates) along the coast of west and northwest Africa.

These aforementioned characteristics of the $dC_{x,y}/dT_{Global}$ multi-model mean should not be considered representative of all CMIP3 models. The range of precipitation change patterns from each of the CMIP3 climate models displays diverse textures (Figures 5 and 6). For example, although a portion of a CMIP3 model's pattern kernels qualitatively displays the west–east

$dC_{x,y}/dT_{Global}$ feature over the southern Nile region (seen most strongly in MAM), some models show a more ubiquitous relative drying whereas others produce the opposite trend (relatively higher precipitation rates). In a similar fashion, a couple of individual CMIP3 model results indicate wetter conditions resulting from climate warming over most of the equatorial region, in contrast to what the multi-model mean result indicates (Figure 4).

Taking into account these characteristics of $dC_{x,y}/dT_{Global}$ in regional precipitation shifts, we then consider the zonal IGSM trends in precipitation in response to increased greenhouse gas concentrations (see Figure 9 of Schlosser et al. 2013). For the southernmost region of the Nile River basin, the interquartile range of zonal precipitation trends are positive, with a small portion of the ensemble producing relatively small negative trends (compared to positive trend counterparts). In the northern portion of the Nile River basin and focus region, although the central tendency of the zonal precipitation trends remains positive, its magnitude drops considerably. In addition, for the northernmost latitudes of the Nile focus region, all zonal trends within the IGSM ensemble are positive.

Temperature

In contrast to precipitation, the model averages of $dC_{x,y}/dT_{Global}$ for T_a (Figure 7) show a very similar trait to that of the 'cold ocean–warm land' (or COWL) pattern (e.g. Broccoli et al. 1998). This pattern is seen for all seasons, but the relative maximum change does vary from season to season. The IGSM produces a zonal profile of warming that is fairly constant across the latitude bands that span this region (see Figure 8 of Schlosser et al. 2013). Therefore, these patterns enhance the zonal warming over the domain. However, the pattern kernels affect the strength of the enhanced regional warming, and the scatter of these patterns across the CMIP3 models is notable (Figures 8 and 9). For most of the models chosen, the pattern kernels produce a stronger regional warming enhancement across the greater Sahel region of northern Africa, as seen by the expansive higher values of $dC_{x,y}/dT_{Global}$ during DJF (Figure 8) and JJA (Figure 9). A notable exception is seen in DJF in which one of the CMIP3 model kernels (and another to a lesser degree) produces an extensive area of buffered warming across most of equatorial Africa. Looking at the precipitation pattern kernels for DJF (not shown), there is a consistency of these buffered warming signatures to relatively higher precipitation rates, which may imply that cloudiness may play a consistent role in the buffered warming.

2.3   Hybrid frequency distributions

By combining the IGSM ensemble of zonal trends with each of the pattern kernels of regional climate change from models of the Fourth Assessment Report of the Intergovernmental Panel on Climate Change (IPCC AR4) (IPCC 2007), we produce a meta-ensemble of climate change projections. As such and hereafter, we refer to these constructions as 'hybrid frequency distributions' (HFDs). In the following sub-section, we present decadal averaged climate changes at 2050 relative to the end of the twentieth century as frequency distributions of the changes. We also focus our presentation and discussion on spring and summer climate conditions as the data will be used as inputs to agricultural and hydrologic impact models in subsequent work. In previous work, the IGSM was used to project climate changes under a UCE pathway (Sokolov et al. 2009) as well as across a range of climate change mitigation policies (Webster et al. 2012). For this study, we focus on a sub-set of these climate projections and consider the UCE case as well as a modest greenhouse gas stabilization scenario in which a CO_2 concentration of ~650 ppm or equivalent is achieved by the end of the century and is referred to as the 'level 2 stabilization' (L2S) policy by Webster et al. (2012).

Looking at the UCE case averaged for the Nile focus region, the HFDs of the DJF area-averaged T_a changes (Figure 10) indicate a mode of temperature change distribution in the range of 2.5–2.75°C by 2050. The distribution is strongly Gaussian in shape, but a slight skew towards higher temperatures is seen. This skewness value is attributed to the fact that some AR4 model pattern kernels impose a stronger warming over the basin (Figures 7a and 9). The L2S climate policy produces a notable reduction in the warming mode by as much as 1.0°C. However, the more notable result is that <5 per cent of the L2S distribution of warming lies in the upper half of the UCE temperature distribution. As a result, only the highest warming with notable likelihood of the L2S distribution coincides with the warming mode of the UCE distribution. Further, approximately 75 per cent of the L2S distribution lies below a 2.0°C warming, whereas about 20 per cent of the UCE distribution occurs at or below this warming. Perhaps the more striking impact of the climate policy scenario is seen in the precipitation results for MAM (Figure 11). Under the UCE pathway, the Nile River basin region exhibits a pronounced mode of increased precipitation likelihoods; however, the total expanse of the distribution covers both decreases and increases in precipitation. Over 60 per cent of the distribution lies at or above the modal increase (note that in all HFD plots of precipitation values are presented in units of millimetre per decad, where 1 decad = 10 days). Conversely, decreases in precipitation only occupy about 15 per cent of the total distribution's population of outcomes. The mode of the UCE distribution contains 31 per cent of the distribution, yet only 12 per cent flanks zero change in precipitation. The effect of the climate policy scenario on HFD is notable. L2S places about 75 per cent of the distribution in the bins that flank a change in precipitation that is less than half the change of the modal UCE value. Moreover, nearly 50 per cent of the distribution now flanks the result of no precipitation change.

Similar results in temperature response are seen for other seasons. For JJA, temperature increases are found to be comparable for the Nile region in the UCE scenario, and the effect of the L2S mitigation scenario places all but 1 per cent of the temperature change distribution below the UCE modal value of change (Figure 12). Further, the likelihood of the L2S modal value and the bins that flank it constitute a larger portion as compared to the DJF result (80 per cent as compared to 70 per cent). Conversely, the effect of the L2S scenario on JJA precipitation distribution change (Figure 13) is much more subtle than that seen for MAM (Figure 11). Overall, the extent (i.e. minimum and maximum values) of distribution and modal value between UCE and L2S results are unchanged. The most salient effect is to increase the likelihood of the modal value of change while reducing the chances of larger changes in precipitation spanned by the UCE distribution.

3   Closing remarks

We have presented results from a hybridized probabilistic technique that produces distributions of potential climatic shifts in precipitation and near-surface air temperature over the Nile River basin and northern Africa. These HFDs are partly based on the MIT IGSM ensembles of a UCE pathway and a modest climate change mitigation scenario. To construct distributions of regional change, the IGSM simulations are combined with climate change pattern kernels based on CMIP3 climate model information, thus resulting in a meta-ensemble. A diagnosis of the pattern kernels and HFDs is provided in support of the impacts assessment work that may use this data.

The climate change pattern kernels for surface air temperature show overall spatial consistency across seasons, and indicate that warming in the Nile River basin and northern Africa is

enhanced with respect to the zonal trend of the IGSM. For precipitation, as gathered from the multi-model average, a majority of these regions in the southeast quadrant of the Nile River basin should experience an enhanced precipitation increase. Corresponding to this increase is a relative decrease in precipitation in the southwest quadrant. This dipole pattern appears most prominent in the MAM and SON periods (northern hemisphere spring and fall). However, these generalizations must be approached with caution, as the collection of pattern change kernels taken from the CMIP3 models exhibit a rich variety in the locations of drier and wetter conditions that in some cases indicate opposite trends to the multi-model mean characteristics noted.

The distributions of precipitation and T_a changes are averaged over the greater Nile River basin region. In addition, HFDs are presented for spring and summer given their importance to agricultural productivity and hydrologic impact; whereas the highest precipitation rates are recorded along the southern flank of the Nile River basin. Overall, the most consistent response to climate policy is seen in the distributions of temperature change. In all seasons, the UCE HFDs indicate that a majority of the outcomes will note warming greater than 2°C by mid-century. Applying the climate policy considered, the total range of HFD outcomes collapse and, perhaps more importantly, much of the distribution of warming falls below 2°C. Further, in all cases temperature warming is reduced by at least 1°C (for spring and summer) and it comprises a larger portion of the total population of the distribution (in most cases about 10 per cent more of the population compared to the UCE HFD scenario).

For precipitation, the most notable effect of the climate policy is seen in MAM and it reduces the occurrence of the largest precipitation changes in terms of both increases and decreases, thereby condensing the total width of the distribution outcomes while also decreasing the modal value of change in half. However, this effect is not seen in other seasons, and in particular for JJA the total distribution range of precipitation change is unaffected by L2S, and the only notable response is an increase in the likelihood of the modal value of change, which is also unaltered by the L2S policy scenario. Further, although these shifts result in an increase in the portion of the population that resides within the modal value of change, the value itself may not differ considerably between UCE and climate policy.

To quantify the risks that these climate change distributions pose, these data need to be vetted through a chain of impact models. Additionally, the large meta-ensembles (6800 members) present a substantial computational demand on any impact assessment that would employ these distributions. As such, techniques that could limit the required HFD sample size while preserving the more important aspects of the distribution are warranted. Such techniques would include, among others, a Gaussian quadrature technique (Arndt et al. 2006).
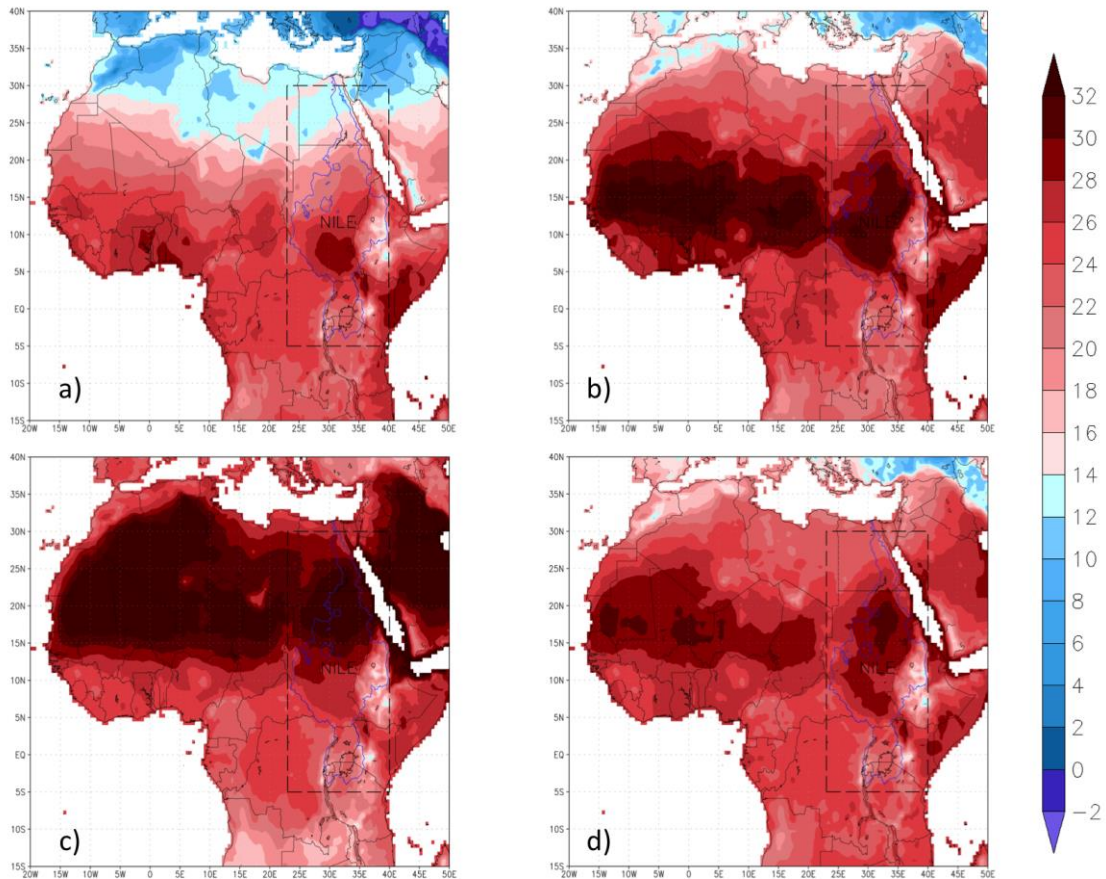
References

Arndt, C., J. Kozlitina, and P.V. Preckel (2006). 'Efficient Survey Sampling of Households via Gaussian Quadrature. *Journal of Royal Statistical Society: Series C (Applied Statistics)*, 55(3): 355–64.

Broccoli, A.J., N.-C. Lau, and M.J. Nath (1998) 'The Cold Ocean–Warm Land Pattern: Model Simulation and Relevance to Climate Change Detection'. *Journal of Climate*, 11(11): 2743–63.

Huffman, G.J., R.F. Adler, D.T. Bolvin, and G. Gu (2009). 'Improving the Global Precipitation Record: GPCP Version 2.1'. *Geophysical Research Letters*, 36(17), 1–5.

IPCC (2007). 'Summary for Policymakers'. In S. Solomon, D. Qin, M. Manning, Z. Chen, M. Marquis, K.B. Averyt, M. Tignor, and H.L. Miller (eds), *Climate Change 2007: The Physical Science Basis. Contribution of Working Group I to the Fourth Assessment Report of the Intergovernmental Panel on Climate Change (IPCC)*. Cambridge/New York: Cambridge University Press. Available at: https://www.ipcc.ch/publications_and_data/ar4/wg1/en/contents.html (accessed 26 December 2015).

Jones, P.D., M. New, D.E. Parker, S. Martin, and I.G. Rigor (1999). 'Surface Air Temperature and Its Variations over the Last 150 Years'. *Reviews of Geophysics*, 37(2), 173–99.

Meehl, G.A., C. Covey, T. Delworth, M. Latif, B. McAvaney, J.F.B. Mitchell, R.J. Stouffer, and K.E. Taylor (2007). 'The WCRP CMIP3 Multi-Model Dataset: A New Era in Climate Change Research'. *Bulletin of the American Meteorological Society*, 88(9): 1383–94.

Schlosser, C. A., X. Gao, K. Strzepek, A. Sokolov, C. E. Forest, S. Awadalla, and W. Farmer (2013). 'Quantifying the Likelihood of Regional Climate Change: A Hybridized Approach'. *Journal of Climate*, 26(10): 3394–414.

Schlosser, C.A., and K. Strzepek (2013). 'Regional Climate Change of the Greater Zambezi River Basin: A Hybrid Assessment'. WIDER Working Paper 2013/040. Helsinki: United Nations University—World Institute for Development Economics Research (UNU-WIDER); also published in *Climatic Change*, 130(2015): 9–19.

Sokolov, A.P., C.A. Schlosser, S. Dutkiewicz, S. Paltsev, D.W. Kicklighter, H.D. Jacoby, R.G. Prinn, C.E. Forest, J. Reilly, C. Wang, B. Felzer, M.C. Sarofim, J. Scott, P.H. Stone, J.M. Melillo, and J. Cohen (2005) 'The MIT Integrated Global System Model (IGSM) Version 2: Model Description and Baseline'. Technical Report Series 124 (40pp). Cambridge, MA: MIT Joint Program on the Science and Policy of Global Change. Available at: http://globalchange.mit.edu/files/document/MITJPSPGC_Rpt124.pdf (accessed 26 December 2015).

Sokolov, A.P., P.H. Stone, C.E. Forest, R. Prinn, M.C. Sarofim, M. Webster, S. Paltsev, C.A. Schlosser, D. Kicklighter, S. Dutkiewicz, J. Reilly, C. Wang, B. Felzer, and H. D. Jacoby (2009). 'Probabilistic Forecast for Twenty-First-Century Climate Based on Uncertainties in Emissions (Without Policy) and Climate Parameters'. *Journal of Climate*, 22(19): 5175–204.

Webster, M., A.P. Sokolov, J.M. Reilly, C.E. Forest, S. Paltsev, C.A. Schlosser, C. Wang, D. Kicklighter, M. Sarofim, J. Melillo, R.G. Prinn, and H.D. Jacoby (2012). 'Analysis of Climate Policy Targets under Uncertainty'. *Climatic Change*, 112(3): 569–83.

Figure 1: Map of the greater region of the Nile River basin

Source: http://en.wikipedia.org/wiki/Nile_Basin. Map created from public domain maps available from the University of Texas.

Figure 2: Seasonal averaged (1979–2009) maps of surface air temperature for northern Africa

Note: Results are shown for (a) December–February (DJF), (b) March–May (MAM), (c) June–August (JJA), and (d) September–November (SON). Units are in degree Celsius. In each frame, the domain indicative of the Nile average is boxed (dashed line) and used for constructing hybrid frequency distributions (HFDs).

Source: Temperature data is based on the Climate Research Unit (CRU, Jones et al. 1999) data archive.

Figure 3: Seasonal averaged maps (1979–2009) of precipitation for northern Africa
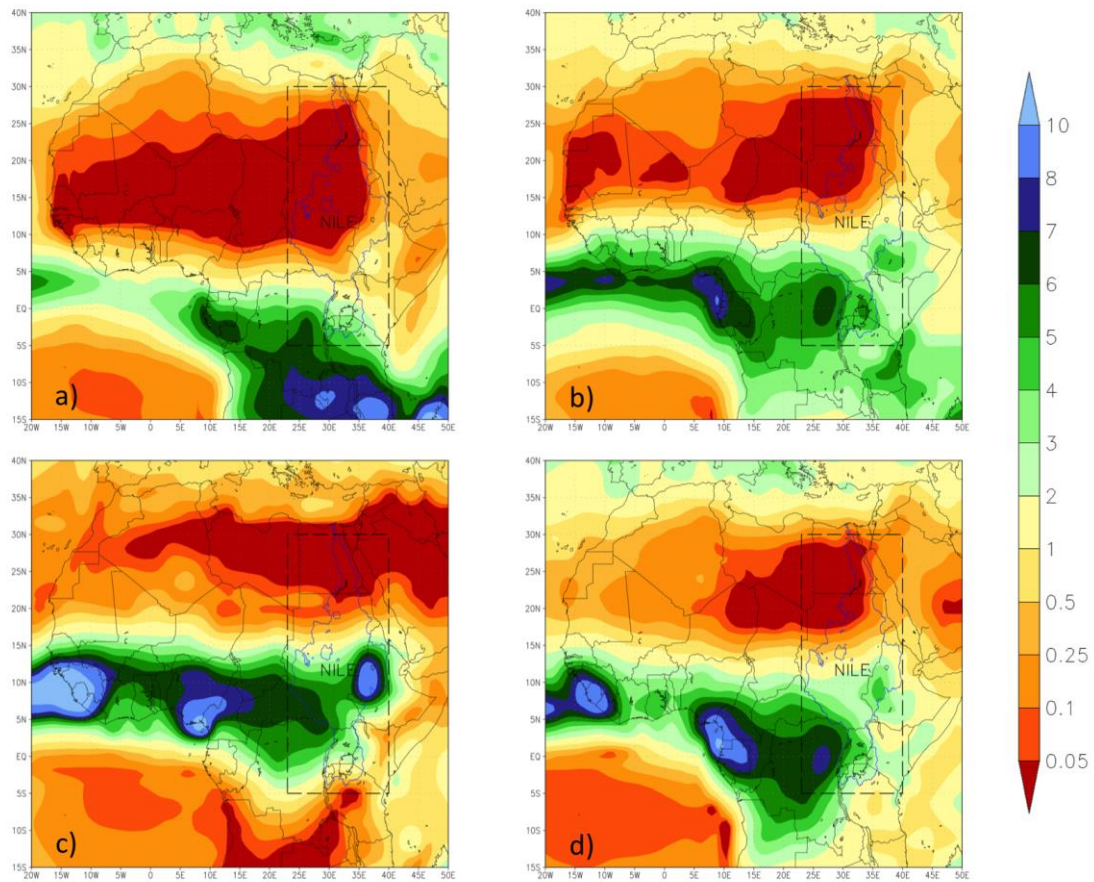
Note: Results are shown for (a) DJF, (b) MAM, (c) JJA, and (d) SON. Units are in millimetre per day. In each frame, the domain indicative of the Nile average is boxed (dashed line) and used for constructing HFDs.

Source: Based on data from the Global Precipitation Climatology Project (GPCP, Huffman et al. 2007).
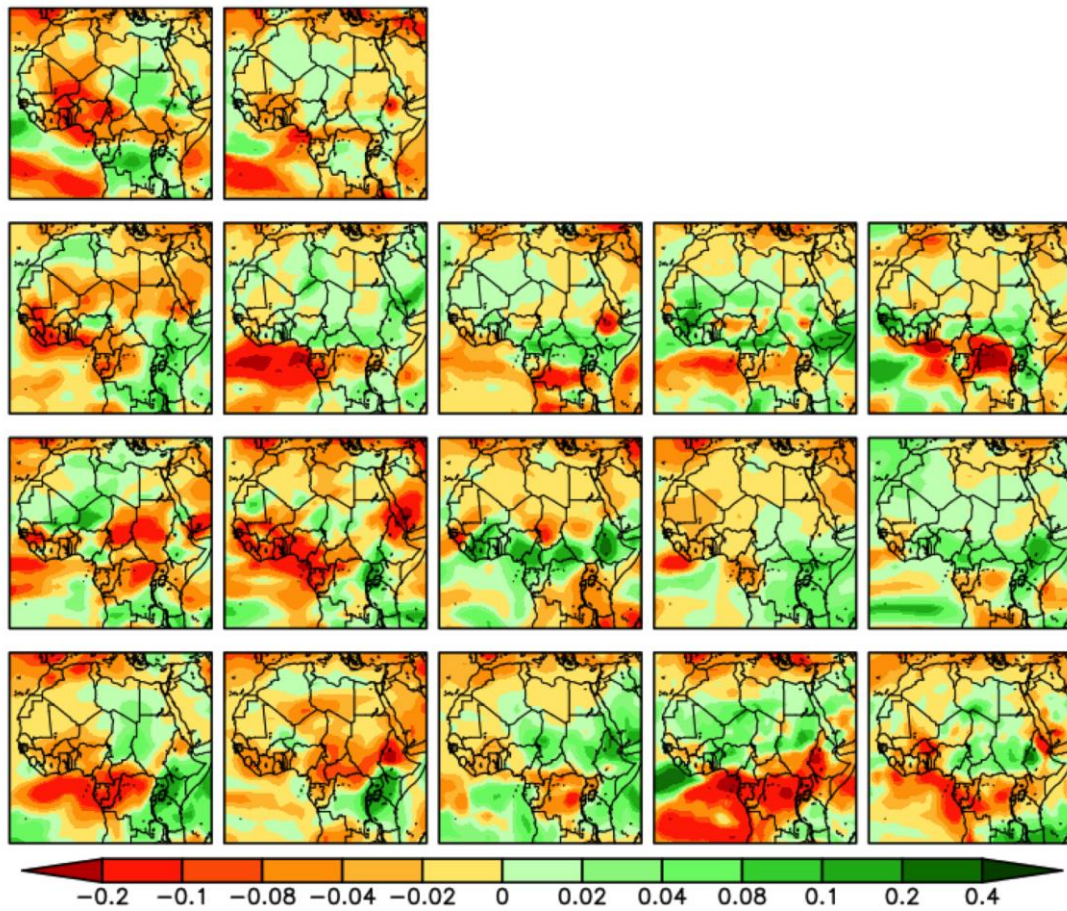
Figure 4: Maps of the transformation coefficients, $dC_{x,y}/dT_{Global}$, for precipitation averaged over results from the IPCC AR4 climate models for northern Africa
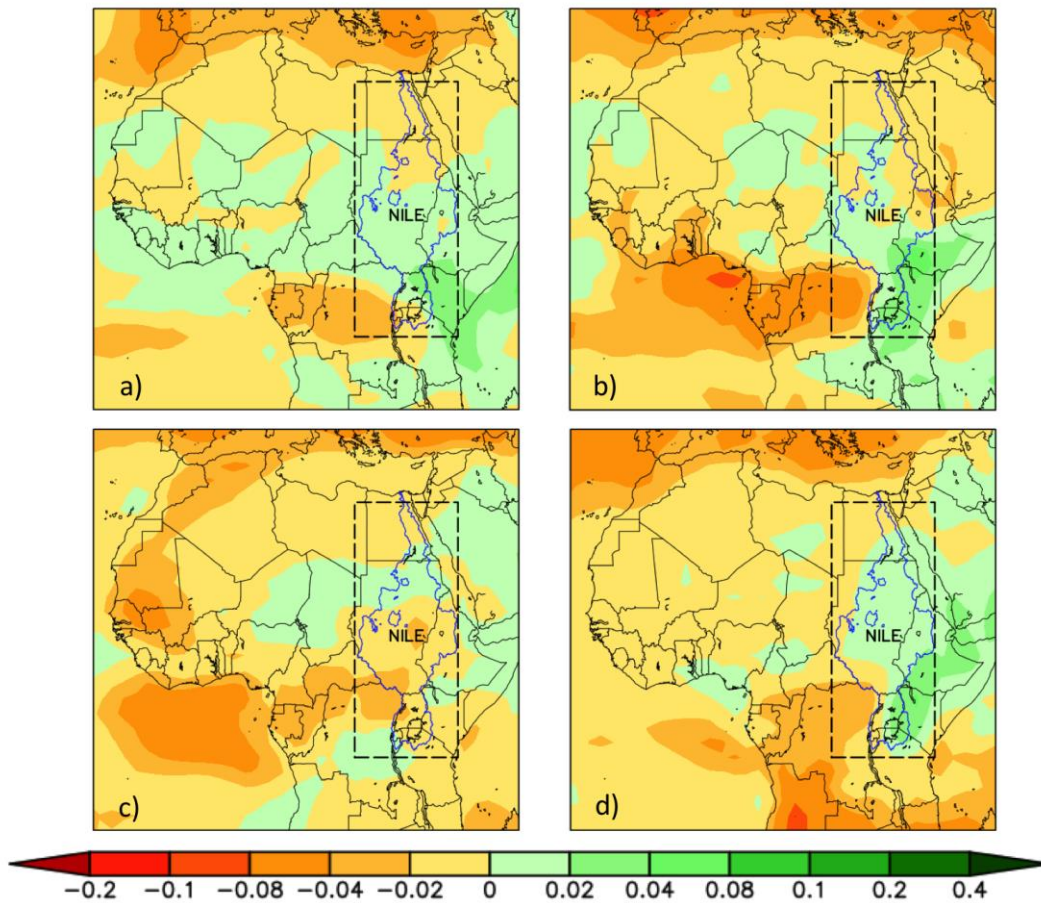
Note: Seasonal pattern shifts averaged for (a) DJF, (b) MAM, (c) JJA, and (d) SON are shown. In each frame, the Nile River basin (blue contour) and the domain indicative of the Nile average (boxed, dashed line) are delineated. Coefficient units are K−1.

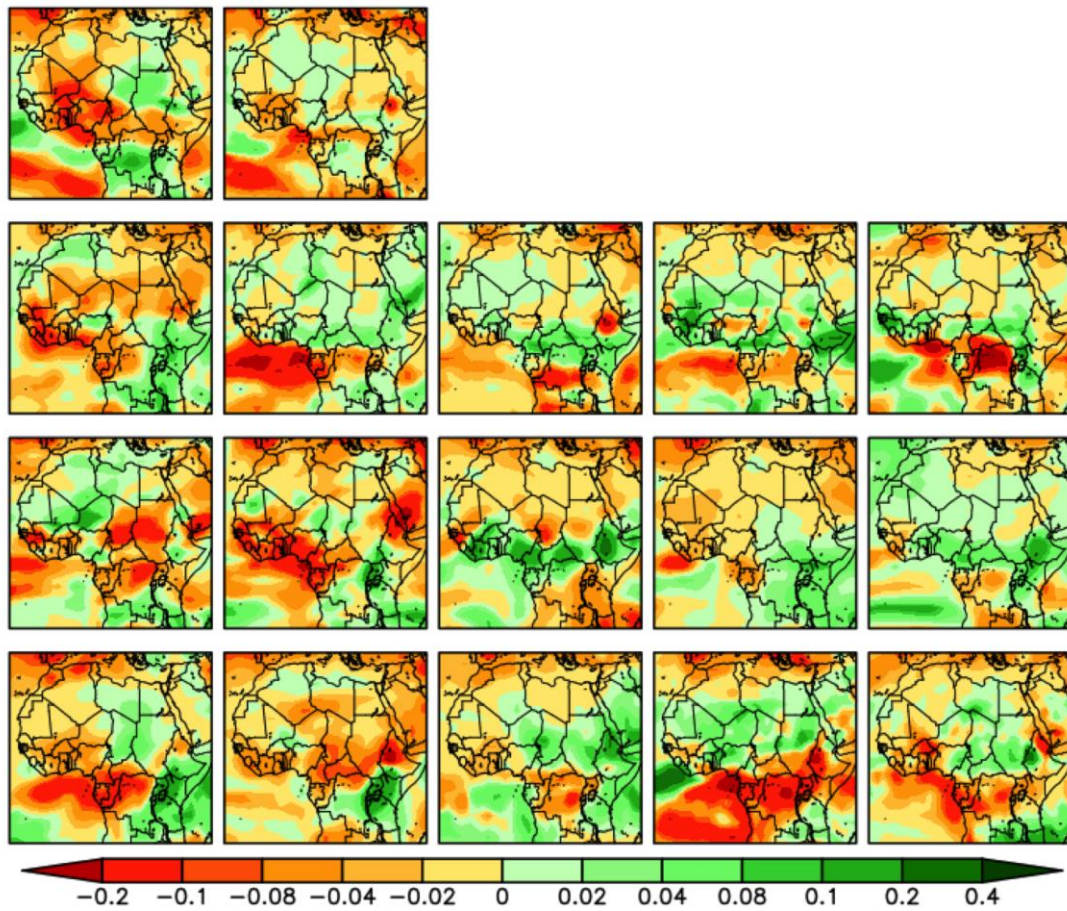Source: Authors' compilation of HFD results using the Nile averaging domain data.

Figure 5: Maps of the transformation coefficients, $dC_{x,y}/dT_{Global}$, for precipitation for northern Africa

Note: Results for each model of the IPCC AR4 collection of the seasonal pattern shifts averaged for MAM. Coefficient units are K−1.
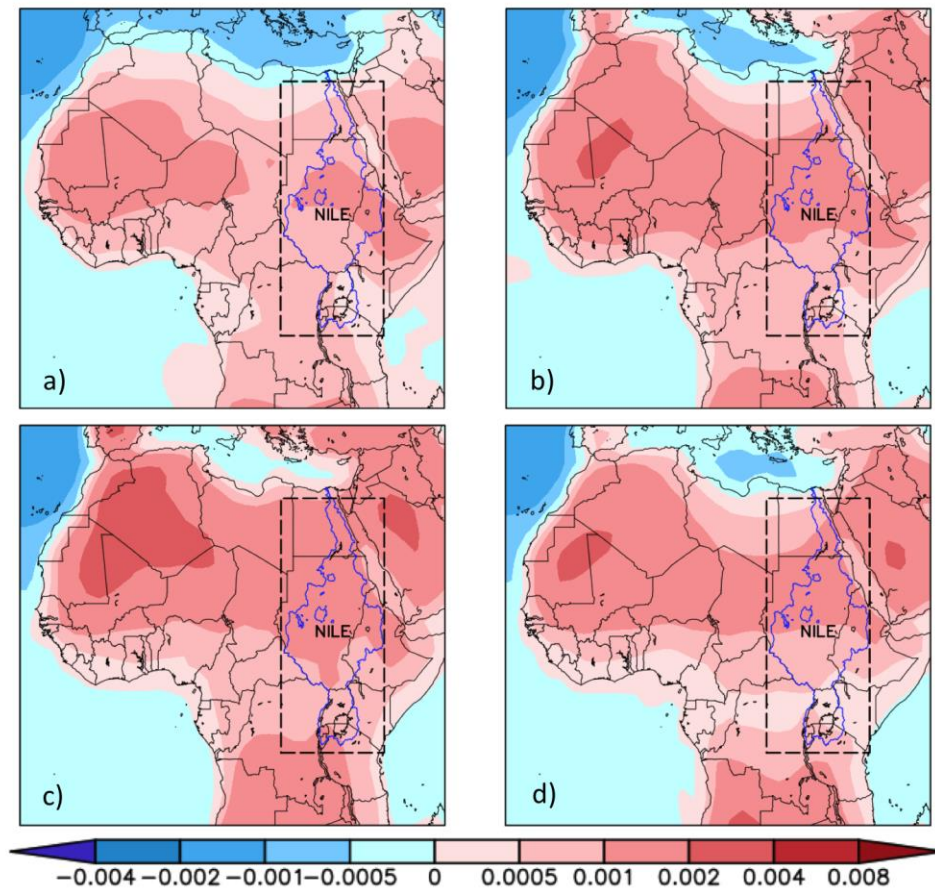
Source: Authors' compilation.

Figure 6: Maps of the transformation coefficients, $dC_{x,y}/dT_{Global}$, for precipitation for northern Africa

Note: Results are shown for each model of the IPCC AR4 collection of the seasonal pattern shifts averaged for JJA. Coefficient units are K−1.
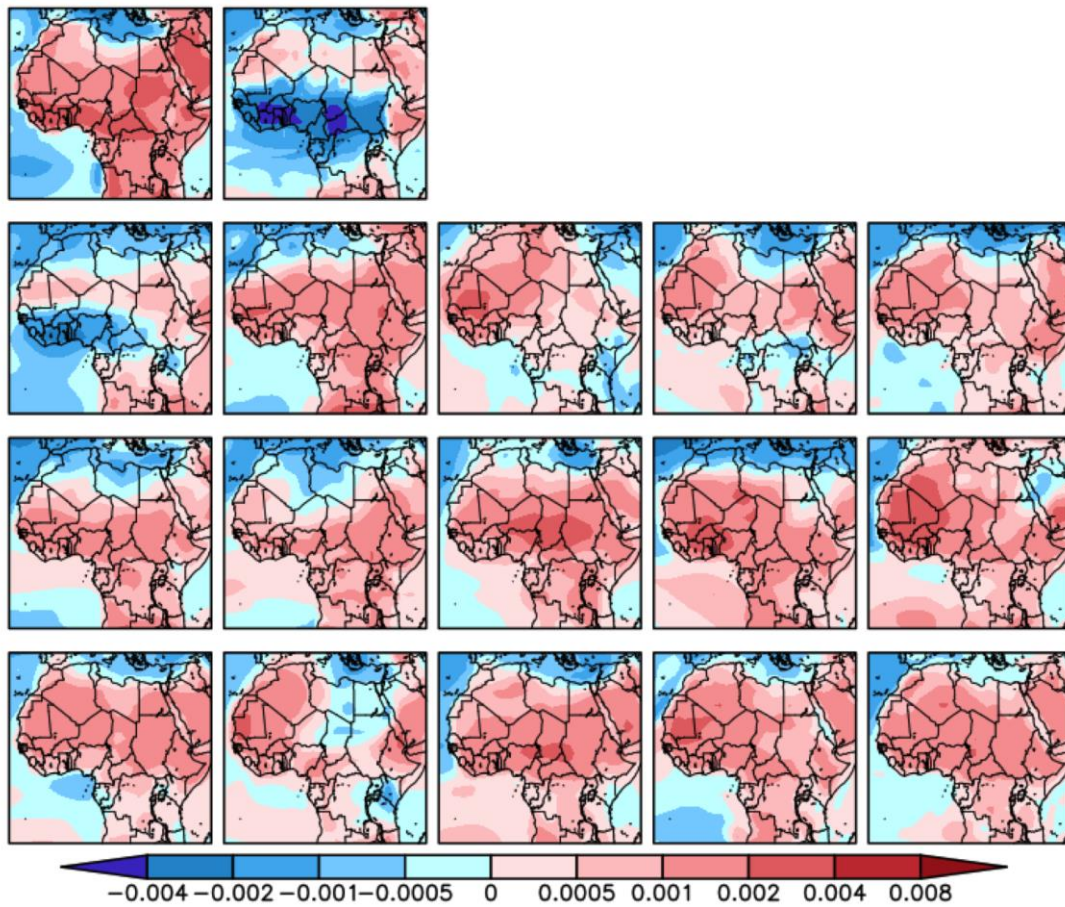
Source: Authors' compilation.

Figure 7: Maps of the transformation coefficients, $dC_{x,y}/dT_{Global}$, for surface air temperature averaged over the results from the IPCC AR4 climate models for northern Africa

Note: Seasonal pattern shifts averaged for (a) DJF, (b) MAM, (c) JJA, and (d) SON are shown. In each frame, the Nile River basin (blue contour) and the domain indicative of the Nile average (boxed, dashed line) are delineated. Coefficient units are K−1.

Source: Authors' compilation of HFD results using the Nile averaging domain data.

Figure 8: Maps of the transformation coefficients, $dC_{x,y}/dT_{Global}$, for surface air temperature for northern Africa
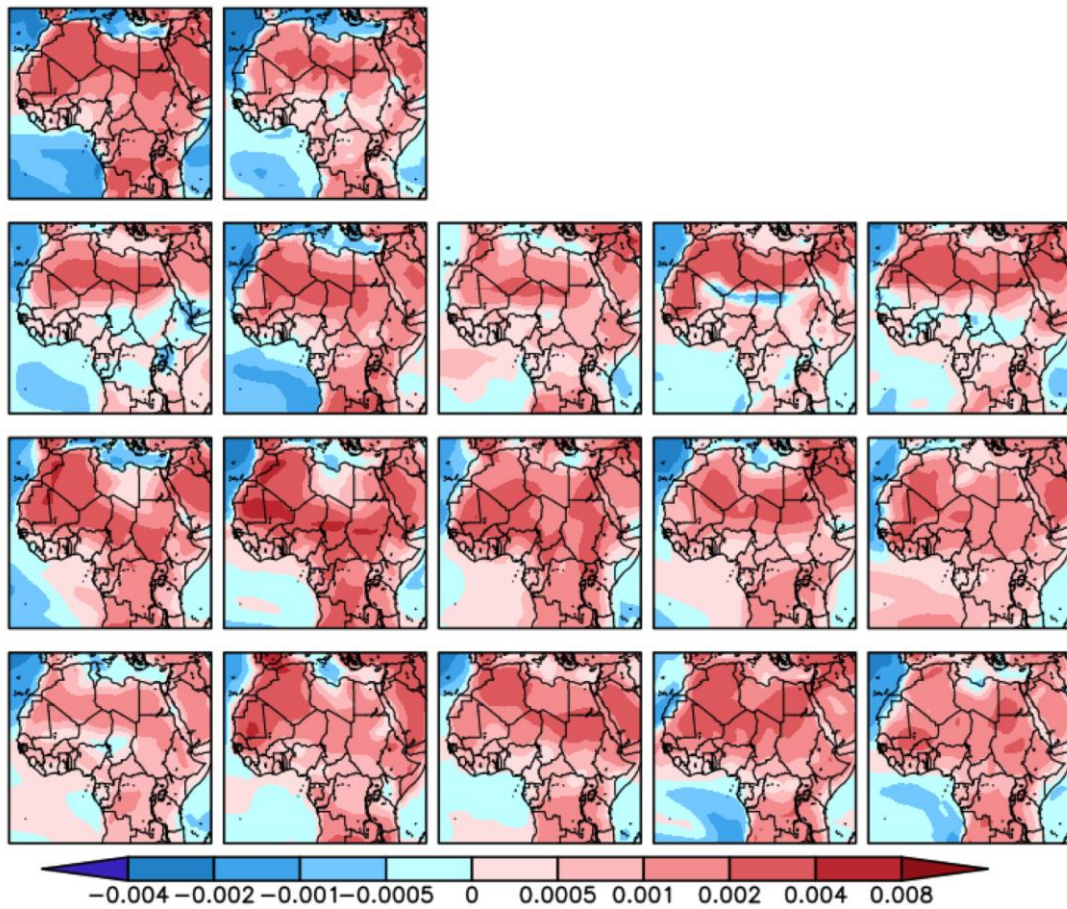

| −0.004 | −0.002 | −0.001 | −0.0005 | 0 | 0.0005 | 0.001 | 0.002 | 0.004 | 0.008 |

Note: Results are shown for each model of the IPCC AR4 collection of the seasonal pattern shifts averaged for DJF. Coefficient units are K−1.

Source: Authors' compilation.

Figure 9: Maps of the transformation coefficients, $dC_{x,y}/dT_{Global}$, for surface air temperature for northern Africa.

Note: Results are shown for each model of the IPCC AR4 collection of the seasonal pattern shifts averaged for JJA. Coefficient units are K−1.
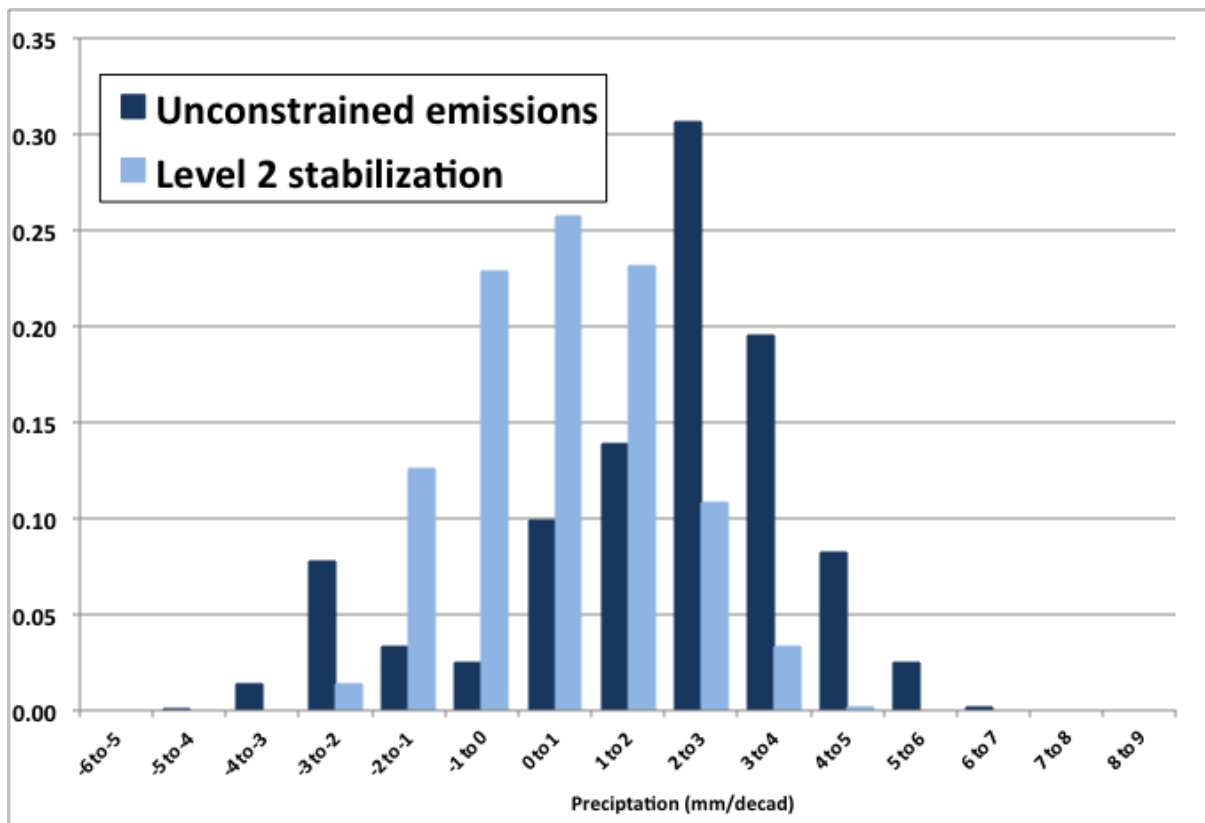
Source: Authors' compilation.

Figure 10: HFDs of decadal averaged DJF mean surface air temperature (T_a) change
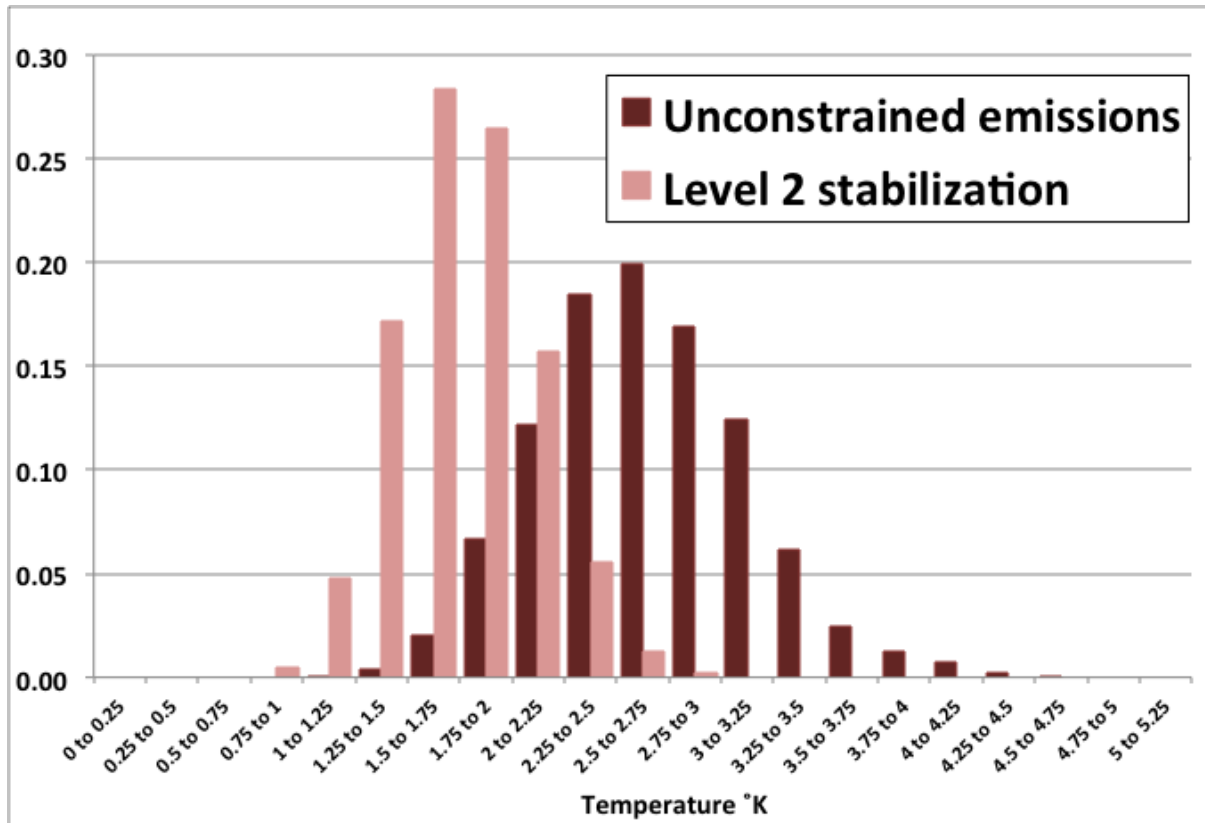
Note: The ordinate values (unitless) depict the fraction of the distribution contained within each corresponding temperature range (denoted in the abscissa labels). The changes are area averaged for the Nile region (boxed area in Figure 7). The decadal averaged changes are shown for 2050, based on the no-policy IGSM ensemble simulation (dark red bars) and the level 2 stabilization scenario (light red bars).

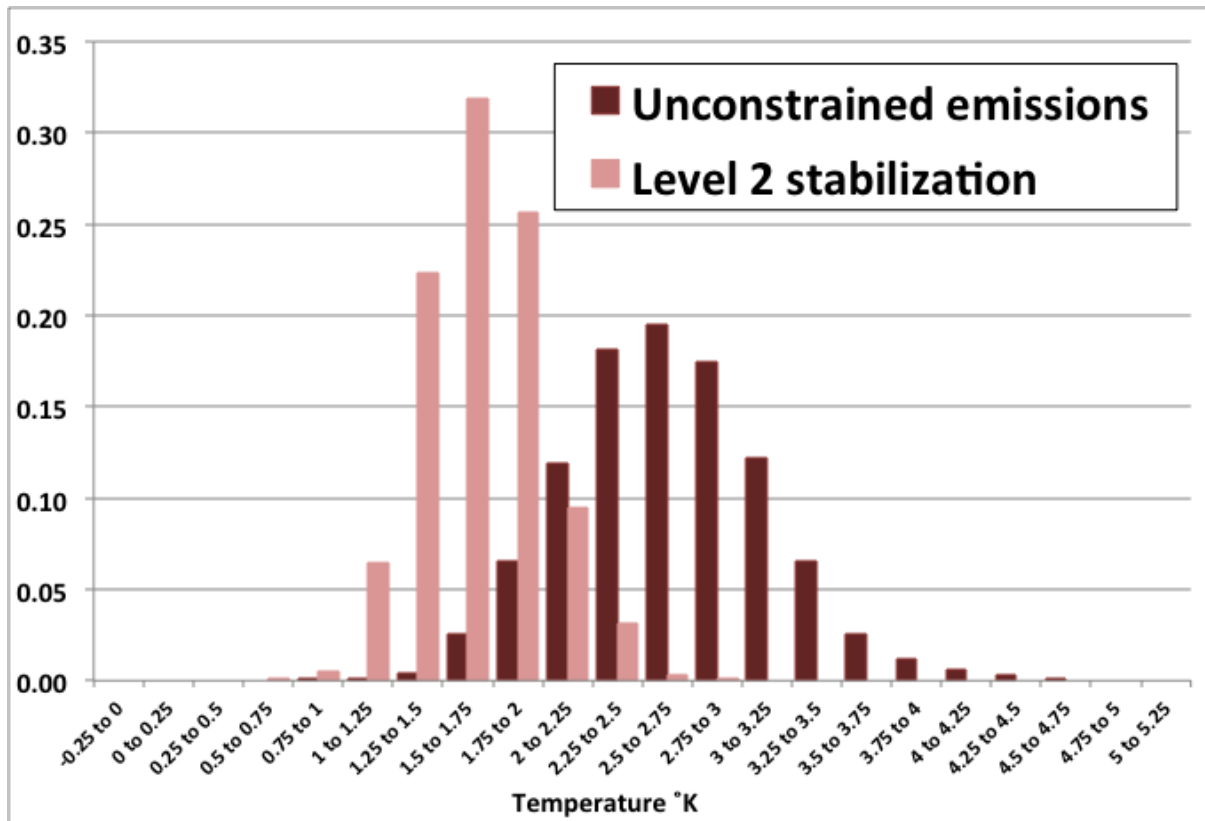Source: Authors' compilation.

Figure 11: HFDs of decadal averaged MAM mean precipitation change

Note: The ordinate values (unitless) depict the fraction of the distribution contained within each corresponding precipitation range (denoted in the abscissa labels). The changes are area averaged for the Nile region (boxed area in Figure 4). Decadal averaged changes are shown for 2050, based on the no-policy IGSM ensemble simulation (dark blue bars) and the level 2 stabilization scenario (light blue bars).
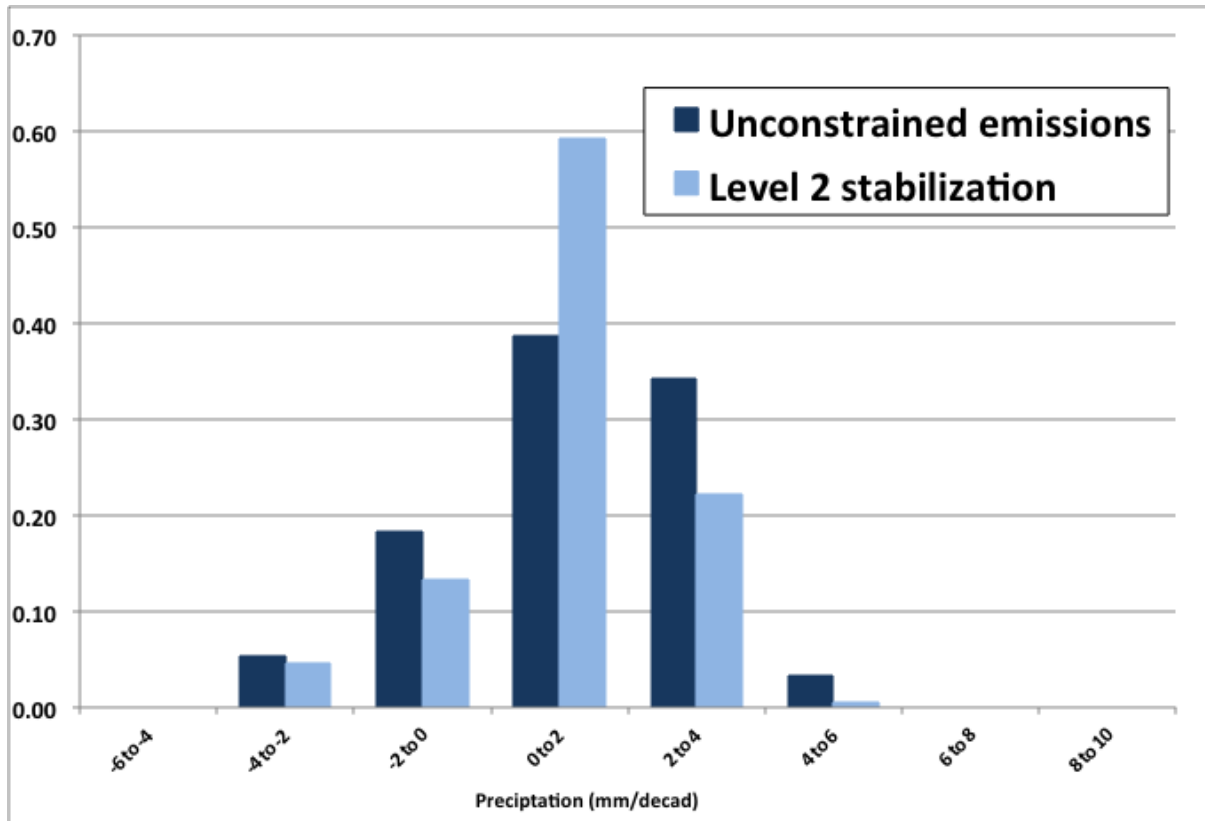
Source: Authors' compilation.

Figure 12: HFDs of decadal averaged JJA mean surface air temperature (T_a) change

Note: The ordinate values (unitless) depict the fraction of the distribution contained within each corresponding temperature range (denoted in the abscissa labels). The changes are area averaged for the Nile region (boxed area in Figure 7). Decadal averaged changes are shown for 2050, based on the no-policy IGSM ensemble simulation (dark red bars) and the level 2 stabilization scenario (light red bars).

Source: Authors' compilation.

Figure 13: HFDs of decadal averaged JJA mean precipitation change

Note: The ordinate values (unitless) depict the fraction of the distribution contained within each corresponding precipitation range (denoted in the abscissa labels). The changes are area averaged for the Nile region (boxed area in Figure 4). Decadal averaged changes are shown for 2050, based on the no-policy IGSM ensemble simulation (dark blue bars) and the level 2 stabilization scenario (light blue bars).

Source: Authors' compilation.